Inorganic Chemistry

Article

pubs.acs.org/IC

Distorted Tetrahedral Co^{II} in $K_5H[CoW_{12}O_{40}]\cdot xH_2O$ Probed by 2p3d Resonant Inelastic X-ray Scattering

Boyang Liu,[†] Ru-Pan Wang,[†] Elliot N. Glass,[‡] Craig L. Hill,[‡] Tanja Cuk,[§] Jun Okamoto,[∥] Di-Jing Huang,[∥] Matti M. van Schooneveld,[*,†] and Frank M. F. de Groot[*,†]

[†]Inorganic Chemistry & Catalysis, Debye Institute for Nanomaterials Science, Utrecht University, Universiteitsweg 99, 3584 CG Utrecht, The Netherlands

[‡]Department of Chemistry, Emory University, Atlanta, Georgia 30322, United States

[§]Department of Chemistry, University of California—Berkeley, 419 Latimer Hall, Berkeley, California 94720, United States

[∥]National Synchrotron Radiation Research Center (NSRRC), Hsinchu 30076, Taiwan

Supporting Information

ABSTRACT: The Co $2p_{3/2}$ X-ray absorption spectroscopy and high-energy-resolution (~0.09 eV fwhm) 2p3d resonant inelastic X-ray scattering (RIXS) spectra of the single-cobalt-centered polyoxometalate $K_5H[CoW_{12}O_{40}]\cdot xH_2O$ were measured. The low-energy dd transition features at 0.55 eV, unmeasurable with ultraviolet−visible (UV/vis) spectroscopy, were experimentally revealed in 2p3d RIXS spectra. RIXS simulations based on ligand-field multiplet theory were performed to assess the potential cobalt tetragonal symmetry distortion, which is described with the ligand-field parameters $10D_q$ (−0.54 eV), D_s (−0.08 eV), and D_t (0.005 eV). Because 2p3d RIXS probes not only the optical spin-allowed transitions but also the spin-forbidden transitions, we show that the current 2p3d RIXS simulation enables a series of dd feature assignments with higher accuracy than those from previous optical data. Furthermore, by wave-function decomposition analyses, we demonstrate the more realistic and detailed origins of a few lowest dd transitions using both one-electron-orbital and term-symbol descriptions.

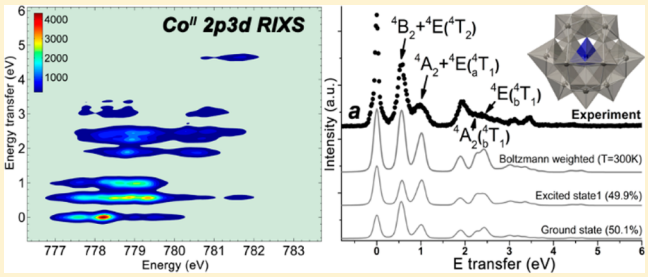

INTRODUCTION

Cobalt-containing materials, in which the cobalt possesses a partially filled 3d shell, exhibit unique electronic and magnetic properties for a wide range of applications. The oxide (α-Al_2O_3, SiO_2, TiO_2, etc.)-supported or carbon-supported cobalt Fischer−Tropsch catalysts are, for example, industrially optimal for the synthesis of long-chain hydrocarbons and clean fuels,[1] while cobalt-doped TiO_2 is of interest for spintronic devices because of its room temperature ferromagnetism.[2] More recently, a series of cobalt-containing polyoxometalates (POMs) have been developed as fast water oxidation catalysts (WOCs)[3−5] to harness the solar energy via artificial photosynthesis. Among the numerous POMs that have been reported as WOCs, POMs containing tetracobalt cores, such as $[Co_4(H_2O)_2(PW_9O_{34})_2]^{10-}$ and $[Co_4(H_2O)_2(VW_9O_{34})_2]^{10-}$, are particularly active.[6] Because cobalt−oxo cores in POMs are suspected of being the active catalytic center,[3] probing the cobalt electronic structure attracts great interest in understanding catalytic behaviors. Single-cobalt-centered POMs are to date found to be catalytically inactive for water oxidation, but the structural similarity of the cobalt−oxo core to those of active POMs makes them important model systems to elaborate on the electronic structure of this class of compounds. To this end, various spectroscopic techniques have been applied, including optical absorption and X-ray absorption (XAS) spectroscopies.[7−11] Owing to the superior discriminative power of 2p3d resonant inelastic X-ray scattering (RIXS),[12] here we probe the electronic structure of 3d-rich cobalt in the single-cobalt-centered POM $K_5H[CoW_{12}O_{40}]\cdot xH_2O$ (originally $K_5H[CoW_{12}O_{40}]\cdot 12H_2O$ vide infra), with an energy resolution better than 100 meV. A large number of dd excitations, including optical-forbidden transitions, were probed. Ligand-field multiplet[13] spectral simulations clearly reveal the presence of Co^{II} ($3d^7$, high-spin) ions in a small tetragonal D_{2d} distorted tetrahedral (T_d) field.

To understand the improvement this work made on the accurate probing and description of the cobalt electronic structure, previous results on α-Keggin $[CoW_{12}O_{40}]^{6-}$ anions are here briefly reviewed with a focus on comparisons to spectroscopic studies. UV/vis absorption and 2p ($L_{2,3}$ edge, 2p to 3d) XAS spectra are mostly used as probes for the 3d-rich electronic structure of cobalt (see ref 12 for a RIXS−XAS−UV/vis comparison of cobalt carboxylates). In UV/vis, dd transitions excited by UV and visible light are used to probe 3d excited states. Commonly, excitations below 1.0 eV (~1240

Received: May 20, 2016
Published: September 27, 2016

DOI: 10.1021/acs.inorgchem.6b01228
Inorg. Chem. 2016, 55, 10152−10160

nm) are not measured. The lack of low-energy dd transitions can be found in UV/vis analyses of $K_2[(C_4H_9)_4N]_4[CoW_{12}O_{40}]\cdot CH_3CN$[7] and $K_5H[CoW_{12}O_{40}]\cdot 15H_2O$,[9] compounds similar to those in the current work. While some advanced spectrometers allow a wider range (longer wavelength range) of detections, low-energy excitations are often masked by vibrational bands of the material. This limitation is seen in the low-energy optical absorption studies on $K_6[CoW_{12}O_{40}]\cdot mH_2O$,[8] in which the expected $^4A_2$ to $^4T_2$ (^4F) transition at 4600 cm^{-1} (~0.57 eV) was not observed because of shadowing by water vibrational bands in the same energy region. Nevertheless, this lowest transition in the T_d cobalt(II) system is important because it effectively reveals the ligand-field parameter $10D_q$.[12] Also, because these dd transitions are the lowest-energy electronic states and, further, involve charge carriers localized to the metal center, catalysis is expected to proceed from them.[14] In the above-mentioned studies, this value could only be theoretically predicted without direct experimental demonstration. Additionally, strong metal-to-metal (cobalt-to-tungsten) or metal-to-ligand (cobalt-to-oxygen) charge-transfer peaks on the high-energy side of UV/vis data shade dd features, while in 2p3d RIXS, dd transitions can be more effectively demonstrated because they can be selectively excited.[15] Other than in UV/vis, in 2p XAS, the 3d empty states are indirectly probed because the final state is dominated by strong 2p3d interactions. Co 2p XAS of $[CoW_{12}O_{40}]^{6-}$ was observed[11] to be featureless mainly because of the final state lifetime broadening, which obscured accurate determination of the electronic structure parameters (e.g., through multiplet analyses). Moreover, various parameter values in multiplet simulations could yield the same 2p XAS shape. This problem was also met in the current 2p XAS simulation, but with the aid of parameters obtained from 2p3d RIXS, the current experimental XAS was well interpreted. Details of the differences in XAS interpretations are discussed. Importantly, both Co 2p XAS and 2p3d RIXS are element-specific, which constrains the probed electronic structure to the suspected catalytic center of the POM. Similar to the advantages of 2p3d RIXS over UV/vis and 2p XAS, as shown for the ligand-field determination of cobalt carboxylates,[12] current RIXS analyses provide more previously unreached details of the cobalt electronic structure in $K_5H[CoW_{12}O_{40}]\cdot xH_2O$. Particularly, by analysis of the low-energy dd transition features, ligand-field multiplet simulations enable a more effective discussion about the potential symmetry distortions of the Co center, which is inaccessible by X-ray diffraction characterization and was only alluded to or assumed based on the limited information from UV/vis spectra.[7,16] Finally, the wave-function decomposition analyses by using ligand-field multiplet projection methods reveal the detailed origins of each dd transition.

EXPERIMENTAL SECTION

General Methods and Materials. $K_5H[Co^{II}W_{12}O_{40}]\cdot 12H_2O$ was prepared according to published procedures and ground to fine powders for analysis.[9,17] The identity, purity, and water of hydration were confirmed by Fourier transform infrared spectroscopy (FT-IR), UV/vis spectroscopy, and thermogravimetric analysis (TGA). IT spectra (2% by weight in KBr) were recorded on a Thermo Nicolet 6700 FT-IR spectrometer. UV/vis spectra were acquired using an Agilent 8453 spectrophotometer equipped with a diode-array detector and an Agilent 89090A cell temperature controller unit. TGA was performed on a PerkinElmer STA 6000 analyzer. Characterizations by UV/vis and FT-IR are provided in Figures S1 and S2.

Sample Preparation for Synchrotron XAS and RIXS Measurements. The blue powder $K_5H[CoW_{12}O_{40}]\cdot 12H_2O$ was pressed into a round pellet (8 mm diameter; <2 mm thickness). FT-IR spectra prior and post pellet formation showed identical spectra, indicating the molecular structure to be unaffected by the process. The pellet was attached with conductive adhesive carbon tape onto an oxygen-free copper holder. The holder was introduced into the load lock chamber, where the pressure was pumped down to 10^{-8} mbar before sample transfer to the main chamber for XAS/RIXS measurements. In vacuum, water molecules could potentially leave the $K_5H[CoW_{12}O_{40}]\cdot 12H_2O$ sample because they are often located in solvent-accessible channels in the crystal structure, which facilitates their evaporation. The number of remaining water molecules largely depends on the ambient pressure, but the FT-IR spectra of the samples upon dehydration under different drying conditions remain identical (not shown). In our case, the number of water molecules left during measurements at 10^{-8} mbar was unclear; thus, we prefer to name the sample as $K_5H[CoW_{12}O_{40}]\cdot xH_2O$ for XAS/RIXS measurements.

XAS and RIXS Measurements. The Co $2p_{3/2}$ XAS spectrum was acquired in the total fluorescence yield (TFY) detection mode by using a photodiode located in the main chamber with a ~90° angle to the incident beam. A linear horizontal (LH, also called depolarized or linear parallel)-polarized beam with a grazing incident angle of ~20° to the sample surface was used for both XAS and RIXS recording. Each XAS spectrum was sampled with 10 points eV^{-1} ranging from 775 to 785 eV. Seven spectra were acquired at pristine sample positions each and averaged to present in this paper. Calibration of the incident photon energy was done at the $2p_{3/2}$ (L_3) edge of a reference CoO single crystal and compared to literature values.[18] During XAS measurements, 50 μm exit slits were opened to optimize and also balance photon counts and the energy resolution (being ~0.5 eV full width at half-maximum, fwhm).[19] The RIXS spectra were measured by the high-energy spectrometer at beamline 05A1 (NSRRC, Taiwan), where the optical system was designed based on the energy compensation principle of grating dispersion.[19,20] For RIXS measurements, the active grating monochromator (AGM) and active grating spectrometer (AGS) need to be kept at the mirror condition, while the energy resolution of RIXS is determined by the width of the entrance slit without being influenced by the width of the exit slit. During the current RIXS acquisition, the entrance slit was set as ~7 μm and the exit slit was opened to 100 μm to increase photon flux, which led to a ~1.0 eV (fwhm) incoming X-ray window on the sample. The outgoing X-ray was focused by the AGS to the CCD detector. The scattering angle between vectors of the incoming and outgoing beams was set to 90°. Measuring RIXS with LH polarization suppresses the cross section of the elastic peak with respect to nonresonant scattering features, and a grazing incident geometry minimizes self-absorption of the elastic peak.[21,22] The RIXS detector was calibrated by positioning the incident beam on the carbon tape and measuring elastic scattering peaks with incoming energies at 780 and 782 eV. Two elastic peaks were fitted with Gaussian functions, and a linear relationship between the fitted maxima was plotted against the detector channels as an energy calibration. Around the Co $2p_{3/2}$ edge (~780 eV) of this POM sample, the RIXS energy resolution of the zero energy transfer peak was ~90 meV fwhm (for details, see the Supporting Information). The RIXS spectra were sampled with 56 points eV^{-1} and at five different excitation energies. The presented RIXS spectra consist of a sum of 30−141 RIXS spectra (1 min acquisition time each). During RIXS acquisition, a new pristine position on the sample surface was exposed each 30 min, a time frame in which no beam damage effects were observed in prior-post comparative XAS and RIXS measurements (prior-post comparative RIXS studies with 1 min acquisition time did also not reveal spectral changes). The pressure and temperature during all XAS/RIXS measurements were $<2.0 \times 10^{-8}$ mbar and room temperature (~300 K), respectively.

DOI: 10.1021/acs.inorgchem.6b01228
Inorg. Chem. 2016, 55, 10152−10160

THEORETICAL BASIS

Multiplet Simulations. XAS and RIXS simulations were performed via the ligand-field multiplet approach using Cowan–Butler–Thole's code, which was further modified and developed by Thole et al.[23−25] This code is implemented in free software interface suites: charge-transfer multiplets for XAS, RIXS, and differential orbital covalency (CTM4XAS, CTM4RIXS, and CTM4DOC).[26,27] In the ligand-field multiplet model, multiplets obtained under atomic symmetry were branched by using group theory to the D_{2d} double group, with the branching route following the $SO_3 > O_h > T_d > D_{2d}$ symmetry groups. This approach, by using atomic multiplets, ligand, and superexchange fields to interpret the origin of 2p XAS and 2p3d RIXS transitions, has successfully simulated a large variety of 3d transition-metal $L_{2,3}$ XAS and 2p3d RIXS.[12,18,28]

In the charge-transfer multiplet model, the effects of charge fluctuations in the initial and final states are taken into account by combining multiple configurations instead of using a single configuration in the atomic or ligand multiplet model. The simulated XAS using this model showed satisfactory consistency to the experimental results of those highly covalent sites.[29] The charge-transfer effects associated with the covalency, however, were neglected in this simulation for ionic Co^{II} sites because each single $2p^63d^7$, $2p^53d^8$, and $2p^63d^8\underline{d}$ configuration is the dominant configuration in the respective states. Here the notation $3d^8\underline{d}$ is used to indicate the possible dd transitions (for the calculation, the $2p^63d^7$ configuration is used). Moreover, in contrast to the X-ray photoelectron spectroscopy (XPS), XAS and RIXS are neutral processes, which implies that only minor charge-transfer effects need to be considered. The omission of charge-transfer effects limits the number of semiempirical parameters used for describing the electronic structures, and it leads to the more precise determination of the ligand-field parameters that are related to the symmetry of Co sites.

We note that the ligand-field multiplet calculation is a semiempirical approach to simulating the 2p XAS and 2p3d RIXS spectral shapes. This approach contains a number of approximations and empirical parameters. The main approximation is that the transition-metal ion is described with a model where only the local 2p and 3d electrons are included. The 2p3d and 3d3d electron–electron interactions and spin–orbit couplings are calculated from first principles for an ion. The crystal-field splitting is used as an empirical parameter, but in this case, the value of $10D_q$ can be directly read from the first dd excitation energy. In addition, small crystal site distortions can be explicitly considered. In our view, it is important to use the ligand-field multiplet model because it captures the essence of the 2p3d RIXS plane in a relatively simple model with a limited number of justifiable parameters.

It is, however, obvious that the semiempirical ligand-field multiplet model is not supposed to replace first-principles calculations. First-principles calculations ultimately will correlate the molecular structure with the electronic structure and subsequently with the excited-state properties such as 2p3d RIXS. It is noted that at this stage first-principles methods are not capable yet of describing the 2p3d RIXS spectra of open-shell systems as accurately as semiempirical codes. This is the case for both the solid-state-based methods of Haverkort et al.[31,32] and Hariki et al.[33,34] and the quantum-chemistry-based methods from the groups of Neese,[35,36] Lundberg,[37] Odelius,[38] and Kühn.[39] The first-principles codes still have difficulties in accurately describing high-spin transition-metal systems with the 90 meV resolution details as visible from 2p3d RIXS.

Ligand-Field Multiplet XAS and RIXS Simulations. A detailed description of the ligand-field multiplet model is given in the Supporting Information,[13,26,40,41] while Table 1 summarizes all of the applied ligand-field multiplet parameters used in the current simulations.

Table 1. Electronic Structure Parameter Values (eV) Used in the Ligand-Field Multiplet Simulations of $2p_{3/2}$ XAS and 2p3d RIXS Spectra of $K_5H[CoW_{12}O_{40}]\cdot xH_2O$

	initial states	intermediate states (RIXS)/ final states (XAS)	final states (RIXS)
Co^{II} configuration	$2p^63d^7$	$2p^53d^8$	$2p^63d^8\underline{d}$
F^2_{dd}	8.077	8.628	8.077
F^4_{dd}	5.018	5.365	5.018
F^2_{pd}		5.518	
G^1_{pd}		4.102	
G^3_{pd}		2.333	
ζ_{3d}	0.066	0.083	0.066
ζ_{2p}		9.748	
$10D_q$	−0.540	−0.430	−0.540
D_s	−0.080	−0.080	−0.080
D_t	0.005	0.005	0.005
Γ(fwhm)		0.400	0.050
G(fwhm)		0.100/0.500	0.090

Descriptions of the Electronic States. The electronic states of transition-metal systems are described with a number of approximate models,[26] which include (i) the one-electron orbital model, e.g., with e and t_2 states in the T_d symmetry or analogous a_1, b_1, e, and b_2 states in the D_{2d} symmetry, and (ii) the term-symbol model, with term-symbol notations in different symmetries. A state represented by a term symbol in lower symmetries (e.g., D_{2d} or D_{4h}) can be decomposed into linear combinations of the atomic or cubic symmetry term symbols.

States of the $3d^7$ initial state and equivalently the 2p3d RIXS final state $3d^8\underline{d}$ are described by term symbols in the D_{2d} double group including the 3d spin–orbit coupling or described by a D_{2d} ligand-field term symbol without considering the 3d spin–orbit coupling effects. Using the projection method[29] implemented in the *CTM4DOC* program, each state is expressed in the atomic and cubic symmetry term symbols and one-electron orbital components. Detailed wave-function expressions of the ground state and a few lowest excited states are presented in Table 2.[30]

RESULTS AND DISCUSSION

Crystal Structure. A polyhedral representation of the α-Keggin $[CoW_{12}O_{40}]^{6-}$ anion is shown in Figure 1a, obtained from a previously published crystal structure (ICSD 427379).[9] The Co^{II} ion can be viewed as encapsulated by the $W_{12}O_{40}$ cage. Four crystallographically determined Co–O bond lengths are 1.898(12) and 1.904(12) Å, with each length for two bonds, as shown in Figure 1b as $Co-O_{(1)}$ and $Co-O_{(2)}$. Similar values can be found in the literature,[9,42] where all four bond lengths are reported as 1.900(12) or 1.895(12) Å. Note that bond lengths derived from X-ray crystallography only reveal bonds of

DOI: 10.1021/acs.inorgchem.6b01228
Inorg. Chem. 2016, 55, 10152−10160

Table 2. Wave-Function Description of the System Ground State and Selected Lowest States

symmetry	energy (eV)	deg	term symbol	atomic composition (%)	cubic composition (%)	orbital composition (%)
SO_3	0.0000	28	^{4}F	100		
	1.6192	12	^{4}P	100		
	1.6265	18	^{2}G	100		
	2.1662	6	^{2}P	100		
	2.1662	22	^{2}H	100		
	2.3536	10	$^2{}_a$D	$21.8\|^2{}_a\mathrm{D}\rangle + 78.2\|^2{}_b\mathrm{D}\rangle$		
	3.7853	14	^{2}F	100		
	5.9464	10	$^2{}_b$D	$21.8\|^2{}_b\mathrm{D}\rangle + 78.2\|^2{}_a\mathrm{D}\rangle$		
T_d	0.0000	4	$^4A_2$	$100\|^4\mathrm{F}\rangle$	$100\|^4A_2\rangle$	$100\|e^4t_2{}^3\rangle$
	0.5399	12	$^4T_2$	$100\|^4\mathrm{F}\rangle$	$100\|^4T_2\rangle$	$100\|e^3t_2{}^4\rangle$
	0.9369	12	$^4T_1$	$97.4\|^4\mathrm{F}\rangle + 2.6\|^4\mathrm{P}\rangle$	$100\|^4T_1\rangle$	$65.8\|e^2t_2{}^5\rangle + 34.2\|e^3t_2{}^4\rangle$
D_{2d}	0.0000	4	$^4B_1$	$100\|^4\mathrm{F}\rangle$	$100\ ^4A_2$	$100\|e^2b_2{}^1a_1{}^2b_1{}^2\rangle$
	0.5400	4	$^4B_2$	$100\|^4\mathrm{F}\rangle$	$100\ ^4T_2$	$100\|e^2b_2{}^2a_1{}^2b_1{}^1\rangle$
	0.5664	8	^4E	$99.5\|^4\mathrm{F}\rangle + 0.5\|^4\mathrm{P}\rangle$	$97.1\|^4T_2\rangle + 2.9\|^4T_1\rangle$	$84.6\|e^3b_2{}^1a_1{}^1b_1{}^2\rangle + 14.2\|e^3b_2{}^1a_1{}^2b_1{}^1\rangle + 1.2\|e^3b_2{}^2a_1{}^1b_1{}^1\rangle$
	0.9400	4	$^4A_2$	$87.6\|^4\mathrm{F}\rangle + 12.4\|^4\mathrm{P}\rangle$	$100\ ^4T_1$	$53.8\|e^2b_2{}^2a_1{}^1b_1{}^2\rangle + 46.2\|e^4b_2{}^1a_1{}^1b_1{}^1\rangle$
	0.9859	8	^4E	$99.4\|^4\mathrm{F}\rangle + 0.6\|^4\mathrm{P}\rangle$	$97.4\|^4T_1\rangle + 2.6\|^4T_2\rangle$	$71.7\|e^3b_2{}^2a_1{}^1b_1{}^1\rangle + 27.0\|e^3b_2{}^1a_1{}^2b_1{}^1\rangle + 1.3\|e^3b_2{}^1a_1{}^1b_1{}^2\rangle$
$D_{2d} + \zeta_{3d}$	0.0000	2	Γ_6	$99.8\|^4\mathrm{F}\rangle + 0.1\|^2\mathrm{G}\rangle$	$97.6\|^4A_2\rangle + 2.2\|^4T_2\rangle + 0.2\|^2T_2\rangle$	$97.6\|e^2b_2{}^1a_1{}^2b_1{}^2\rangle + 1.4\|e^2b_2{}^2a_1{}^2b_1{}^1\rangle + 0.8\|e^3b_2{}^1a_1{}^1b_1{}^2\rangle + 0.2\|e^3b_2{}^1a_1{}^2b_1{}^1\rangle$
	0.0006	2	Γ_7	$99.8\|^4\mathrm{F}\rangle + 0.1\|^2\mathrm{G}\rangle$	$97.8\|^4A_2\rangle + 2.0\ \|^4T_2\rangle + 0.2\|^2T_2\rangle$	$97.8\|e^2b_2{}^1a_1{}^2b_1{}^2\rangle + 1.5\|e^3b_2{}^1a_1{}^1b_1{}^2\rangle + 0.4\|e^3b_2{}^1a_1{}^2b_1{}^1\rangle + 0.2\|e^2b_2{}^2a_1{}^2b_1{}^1\rangle$

[a]Columns 1−4: point group symmetries, energies of the states, degeneracies of the states, and the term-symbol representation of the states in the corresponding symmetries. Columns 5−7: compositions of the states in atomic term symbols, cubic symmetry term symbols, and one-electron orbitals. Calculations in each point-group symmetry are all based on ligand-field multiplet parameters listed in Table 1.

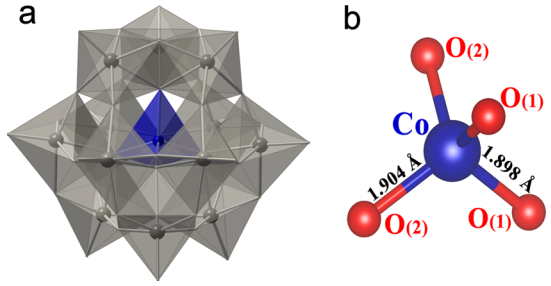

Figure 1. (a) X-ray crystal structure of the $[CoW_{12}O_{40}]^{6-}$ anions in polyhedral representation (the cobalt−oxo core is in blue, and the tungstate octahedra are in gray). (b) Ball-and-stick representation of the core Co ion coordinated with four O ions. Experimental (crystallographic) bond lengths (Å): Co−$O_{(1)}$ = 1.898(12); Co−$O_{(2)}$ = 1.904(12).

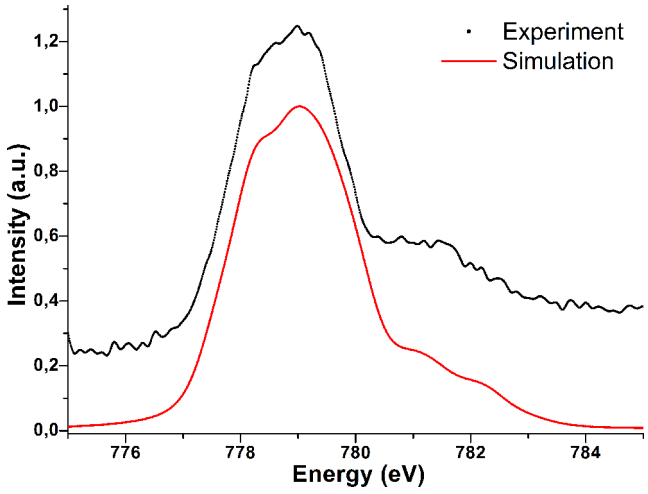

Figure 2. Experimental (black dotted line) and simulated (red solid line) Co $2p_{3/2}$ XAS (TFY) of $K_5H[CoW_{12}O_{40}]\cdot xH_2O$.

the crystalline sample, and the information obtained is limited by symmetry-derived crystallographic disorder.

XAS Experiment and Simulation. The experimental Co $2p_{3/2}$ XAS (TFY) of $K_5H[CoW_{12}O_{40}]\cdot xH_2O$ and the corresponding ligand-field multiplet simulation are shown in Figure 2. The simulation was performed using parameters listed in Table 1. The ligand-field parameter $10D_q$ was found to be −0.54 and −0.43 eV (a negative value is used in the T_d symmetry) for ground states and core−hole excited states, respectively. The initial state $10D_q$ is obtained with high certainty (<5% error) from the RIXS data and the excited-state value from the XAS data (see Figure S3 and its discussion for details). We ascribe the decreased crystal field in the excited state to the 2p core−hole localization of the 3d electrons, thereby decreasing the overlap with the O 2p orbitals.[43] The electron interactions were scaled to effectively include the screening effect of solids.[24] Here, the scalings of 3d3d (F_{dd}) and 2p3d (F_{pd} and G_{pd}) interactions were set to 87% and 95% of their atomic values, respectively. The scaling of the F_{dd} parameter is obtained accurately (~2% error) from the RIXS data, as explained in Figure S4 and its discussion. The reduction of the 3d3d interactions is approximately twice that of the 2p3d interactions because they contain two valence electrons. Through these parameter determination methods, a well-simulated $2p_{3/2}$ XAS spectrum was achieved, as shown in Figure 2.

The presented experimental spectrum varies from a previously reported $2p_{3/2}$ XAS obtained on the same sample but which was measured in the total electron yield mode.[11] The observed spectral shape difference may result from a number of factors: (i) TFY-detected XAS is a bulk probe[44] and, as such, is less sensitive to surface effects compared to electron yield detection (additionally, potential beam-induced effects are

DOI: 10.1021/acs.inorgchem.6b01228
Inorg. Chem. 2016, 55, 10152−10160

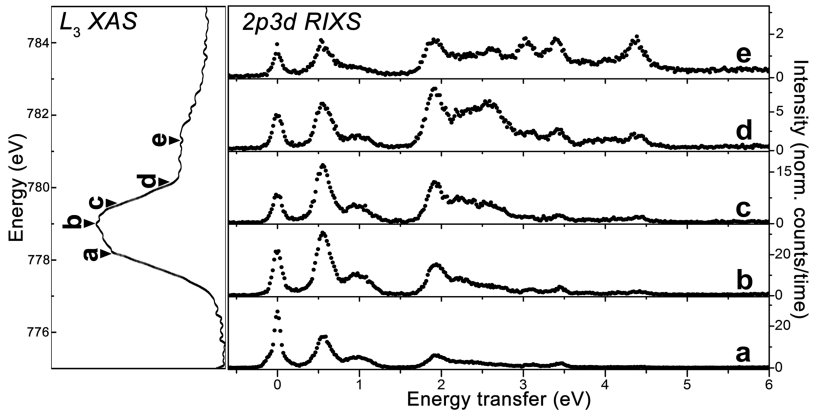

Figure 3. Experimental Co $2p_{3/2}$ XAS (left) and 2p3d RIXS (right) spectra of the $K_5H[CoW_{12}O_{40}]\cdot xH_2O$ POM, both acquired at 300 K with an LH-polarized incident beam. The five RIXS spectra were acquired at excitation energies a–e indicated at the XAS spectrum.

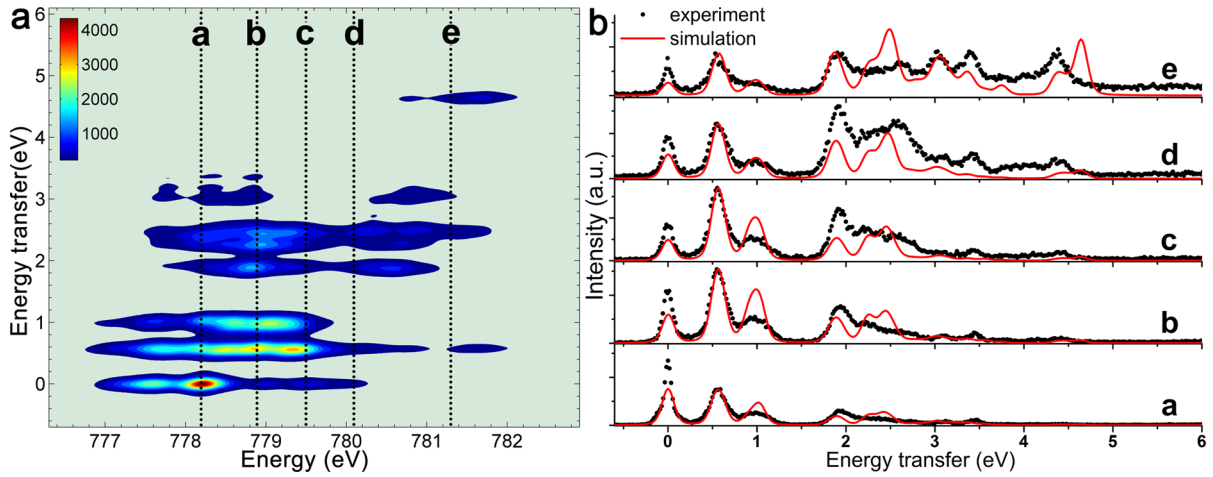

Figure 4. (a) Ligand-field multiplet 2p3d RIXS plane of Co^{II} in $K_5H[CoW_{12}O_{40}]\cdot xH_2O$. The black dotted lines correspond to the centers of ~1 eV fwhm excitation bands a–e (see Figure 3). (b) LH-polarized experimental (black dotted line) and corresponding ligand-field multiplet (red solid line) RIXS spectra at excitation energies a–e.

strongest at the surface[45]). (ii) Potentially, TFY is sensitive to saturation effects, but the low cobalt loading and the presence of 12 heavy W atoms for each cobalt likely prevent any detectable saturation effects. (iii) Different experimental XAS broadenings appear in the different experiments.

RIXS Experiment and Simulation. The experimental $2p_{3/2}$ XAS and 2p3d RIXS spectra are shown in Figure 3. In the XAS panel (left), excitation energies chosen for RIXS measurements are indicated by arrows a–e. This a–e letter denomination is applied in the whole text. Note here that energy positions a–e represent the centers of incident energy windows of approximately 1.0 eV fwhm (see the Experimental Section). The corresponding 2p3d RIXS spectra (right panel) are intensity-normalized to the acquisition time. The 2p3d RIXS probed at the Co $2p_{3/2}$ edge carries the information on the elastic scattering and elementary excitations including dd, charge-transfer (ligand-to-metal and metal-to-ligand), magnon, and phonon (<100 meV) excitations.[46] Low-energy phonon and magnon excitations of the $^4A_2$ ground state are invisible because the experimental resolution of 90 meV is larger than their excitation energies. However, phonons and magnons could lead to a broadening of the elastic peak related to the $^4A_2$ ground state, as well as additional broadening of the dd excitations to the $^4T_1$ and $^4T_2$ states. Charge-transfer excitations are typically minor for Co^{II}–O_x species[18] and broader than the observed features, especially at excitation energy e, where they appear relatively strong. The main energy-transfer spectral features are thus ascribed to dd excitations. From the five RIXS spectra, it can be found that (i) spectral features appear at fixed energy transfer exhibiting their dd excitation nature, (ii) the intensity ratio between the dd features changes with the excitation energy, and (iii) more dd features are observed at higher energy transfer in RIXS spectra acquired at higher excitation energies.

The ligand-field multiplet simulation of the Co^{II} 2p3d RIXS spectra employed the parameters listed in Table 1. The simulation (at 300 K) of the full RIXS transition process from $2p^63d^7$ to $2p^53d^8$ and then to $2p^63d^8\underline{d}$ yields the two-dimensional (2D) plane shown in Figure 4a. In this 2D RIXS plane, the energy transfer ($\Omega-\omega$) is plotted against each incident/excitation energy (Ω) over the Co $2p_{3/2}$ edge. The incident energy of this generated 2D plane was shifted to fit with the energies of the experimental XAS. To simulate the experimental incident beam, 1 eV fwhm Gaussian-broadened incident energy bands (Ω'), centered at a–e, were used. The five selected cross sections $I(\Omega'-\omega)|_{\Omega'}$ were plotted against their respective experimental spectra in Figure 4b. Here, the simulated spectra were normalized to the intensity of the first experimental dd peak (at ~0.55 eV). Although the scaling factor for each simulated RIXS cross section is now slightly

DOI: 10.1021/acs.inorgchem.6b01228
Inorg. Chem. 2016, 55, 10152–10160

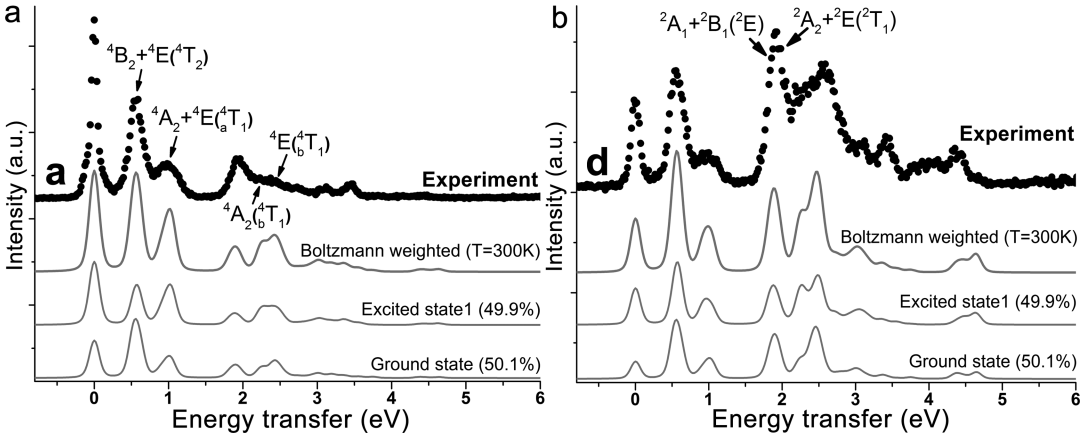

Figure 5. Experimental (black dots) and corresponding ligand-field multiplet (gray lines) RIXS spectra at excitation energies a (panel a) and d (panel b), respectively. The theoretical ground and first excited state RIXS spectra are shown, together with their Boltzmann-weighted sum at 300 K (spectral weights in brackets). The ligand-field multiplet-obtained symmetry labels of selected dd manifolds in D_{2d} and T_d (in brackets) symmetry are indicated.

different (ratio varying between 1.0 and 1.8), this procedure allows a straightforward comparison between the inelastic features of the theoretical and experimental results. The normalization method is justified because each spectrum was either measured at a new sample position or an averaged result from spectra measured at several positions (cf. the Experimental Section), with a varying surface roughness. The surface roughness can lead to additional intensities due to reflectivity.

Overall, the simulated RIXS spectra reproduce the energy positions of the dd peaks well, especially in the energy-transfer region below 2 eV. The dd features at 3.06 and 3.36 eV are also reproduced especially in spectrum e, although an additional feature at higher energy transfer is observed in the simulation. This is potentially a result of ignoring charge-transfer effects in the current simulation because charge transfer mainly affects high-energy-transfer features.[15,18]

On the basis of the ligand-field multiplet calculations, a few selected dd excitations were labeled in Figure 5 with D_{2d} and T_d (in brackets) symmetry term symbols. The peak at 0.55 eV corresponds to the $^4T_2$ excited state in the T_d symmetry, which is further split into $^4B_2$ and ^2E states because of the tetragonal D_{2d} distortion. The dd peak at ∼1 eV contains two dd transitions: the ground-state $^4B_1$ to the $^4A_2$ and ^4E states. Similarly, the two states are split from the $^4T_1$ state in the T_d symmetry. This ∼1 eV $^4T_1$ state, indicated in Figure 5 as $^4_aT_1$, represents the $^4T_1$ state originating from the atomic multiplet ^4F, and $^4_bT_1$ represents the $^4T_1$ state from the atomic multiplet ^4P. The $^4B_1$ to $^4A_2$ ($^4_bT_1$) and ^4E ($^4_bT_1$) transitions are at ∼2.24 and ∼2.43 eV (Figure 5a), respectively. The calculations show that the broad peak at ∼1.93 eV consists of four doublets: $^2A_1$, $^2B_1$, $^2A_2$, and ^2E in D_{2d} symmetry (originating from the ^2E and $^2T_1$ states in the T_d symmetry, as shown in Figure 5b).

Similar excited states have been determined from optical spectra and density functional theory (DFT) calculations of the $[CoW_{12}O_{40}]^{6-}$ anions.[7−9,16] The optical absorption measurable features at 7.8 × 10^3 cm^{-1} (∼0.97 eV) and 16 × 10^3 cm^{-1} (∼1.98 eV) were in T_d symmetry assigned to the spin-allowed transitions of the $^4A_2$ ground state to the $^4_aT_1$ and $^4_bT_1$ states.[7,9] Equivalent assignments can also be found in the optical absorption and emission data of T_d Co^{II} sites in $MgAl_2O_4$.[47] Naturally, for different T_d Co^{II} sites, different transition energies are found. The main difference between the optical absorption and 2p3d RIXS is that the relative intensities of the dd excitations are different in 2p3d RIXS, partly because the spin-forbidden transitions have intensity equivalent to that of the spin-allowed transitions.

Boltzmann-Weighted RIXS Simulation. As stated previously, the ligand-field multiplet simulations for XAS and RIXS were both performed by taking into account the temperature-dependent occupation of the excited states. All experimental spectra were acquired at 300 K, and ligand-field multiplet analysis indicated that the spectral weight from the ground and first excited states needs to be considered. The spectral effect of summing Boltzmann-weighted excited states with the ground state was demonstrated for CoO 2p3d RIXS,[18] in which the first five states account for 93% of the room temperature populated states. Here, the energy difference between the ground and first excited states was calculated to be ∼0.6 meV. These two states account for ∼100% of the room temperature populated states, where the population percentage of the first excited state is ∼49.9% (the occupation fraction $p_i = \exp[-\Delta E_i/kT)/\sum_j \exp(-\Delta E_j/kT]$, with k being the Boltzmann constant). RIXS simulations for the ground state, the first excited state, and the Boltzmann-weighted spectra at 300 K, along with the respective experimental spectra at excitation energies a and d, are shown in Figure 5. A comparison of excitation energies b, c, and e is given in Figure S5. The simulated RIXS spectra of the ground and first excited states are similar, except for minor different intensity ratios between the dd features. This results from the different intermediate states that the ground and the excited states reach.

Investigation of the D_{2d} Co^{II} Site Distortion. The present RIXS data suggest that the Co^{II} site is distorted in the α-Keggin $[CoW_{12}O_{40}]^{6-}$ anion. Figure 6 shows the low-energy-transfer features of simulated 2p3d RIXS spectra in T_d and D_{2d} symmetries in comparison with the experimental results. The calculations represent room temperature spectra (Boltzmann weighting included), and their parameters are listed in Table S1. The deliberately applied, too small final state broadening allows one to view the 3d spin−orbit-coupling-induced splittings of the $^4T_2$ peak at ∼0.55 eV and the $^4T_1$ peak at ∼1.0 eV in T_d symmetry and the additional splittings in D_{2d} symmetry. In our calculations, the 3d spin−orbit coupling is unquenched and thus at its atomic value. Even for this

DOI: 10.1021/acs.inorgchem.6b01228
Inorg. Chem. 2016, 55, 10152−10160

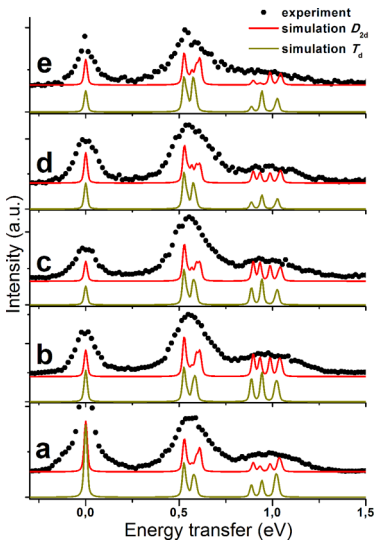

Figure 6. Low-energy-transfer 2p3d RIXS spectral cross sections at excitation energies a–e: experiment (black dots) and simulations in T_d (dark-yellow solid lines) and D_{2d} (red solid lines) symmetries.

maximum value, it alone cannot account for the broadening of the $^4T_2$ and $^4T_1$ peaks. Including the D_{2d} site distortion, an improved agreement is found for broadening of the $^4T_2$ peak in spectra a–e, the asymmetric shape of the $^4T_2$ peak (especially for spectrum c), the spectral weight distribution of the $^4T_1$ peak for all spectra, and the relative intensity ratio between the $^4T_2$ and $^4T_1$ peaks (especially for spectra a and b). Note that Figure 4b gives a comparison of the calculation in D_{2d} symmetry to the experiment, using appropriate broadenings. From Figure 6, it can now be seen that a description of the system in pure T_d symmetry would lead to almost equal intensity ratios of the $^4T_2$ to $^4T_1$ peaks in spectra a and b, which is not the case in the experiment. This relative intensity ratio is also not likely to be influenced by phonons (an alternative reason for broadening of the $^4T_2$ and $^4T_1$ peaks) because both peaks are likely to have similar vibrational couplings (both quartet in nature). The here-obtained distortion parameters are D_s = −0.08 eV and D_t = 0.005 eV. The exact values of the distortion parameters are difficult to obtain from the RIXS spectra with the current resolution, but in the Supporting Information and Figure S6, it is explained how these parameters were obtained precisely. Using the derived D_s and D_t values, the point charge model,[49] and a Co^{II} radius of 72 pm,[50] we obtain two sets of Co–O distances of 1.89 and 1.90–1.97 Å, roughly in agreement with the 1.898(12) and 1.904(12) Å values found by X-ray crystallography.[9] Note that the accuracy in the numbers obtained from crystallography is much higher than those obtained from the point-charge model (LFM/RIXS) but that there is a difference between X-ray diffraction and X-ray spectroscopy regarding symmetry distortions. Spectroscopy measures the energy position of the states that are determined by the point group, while diffraction measures the symmetry distortions in the unit cell of the space group. This implies that if the distortion is not ordered, it will not be visible in diffraction, while in 2p3d RIXS, such unordered distortions will be visible in the energy position shifts. Despite our solid arguments in favor of the presence of a Co^{II} site distortion, the present experimental resolution cannot definitively establish it, especially when it comes to exact determination of the D_s and D_t values. The experimental resolution of Co 2p3d RIXS has been improved to around 20 meV at the new beamline ID 32 in the European Synchrotron Radiation Facility (Grenoble, France) and with a 20-meV-resolved experiment, the cobalt symmetry distortions would be more clearly and accurately probed.

Energy Levels under the Atomic Multiplet, Tetrahedral Field, Tetragonal Distortion, and 3d Spin–Orbit Coupling. Figure 7 shows the energetic levels of the ground and selected excited states due to atomic multiplets, tetrahedral crystal fields, tetragonal crystal fields, and 3d spin–orbital coupling. Energy values of most presented states are listed in Table 2. In the spherical symmetry (SO_3), the 28-fold ^4F multiplet state is the ground state. Note that the energy difference of the ^4P and ^2G states was calculated to be 7.3 meV, which renders the states indistinguishable in Figure 7. The ^2P and ^2H multiplet states were calculated to be the 28-fold degenerate[48] at 2.17 eV above the ground state. In the second panel (from the left), the atomic multiplet states are branched in tetrahedral symmetry ($10D_q$ = −0.54 eV). The 4-fold $^4A_2$ multiplet state, branched from the ^4F state, forms the ground state, while $^4T_2$ and $^4T_1$ are the first two excited states. The $^4A_2$ state further branches to the $^4B_1$ state under tetragonal (D_{2d})

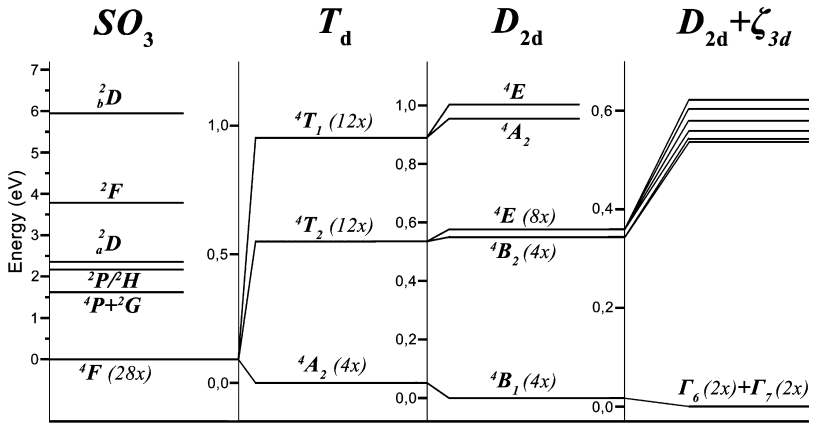

Figure 7. From left to right: branching of the Co^{II} energy levels due to atomic multiplet effects (spherical SO_3 symmetry), followed by branching in tetrahedral T_d and tetragonal D_{2d} symmetric ligand fields, followed by the application of 3d spin–orbit coupling ζ_{3d}. The energy of the ground state is set to zero in each scheme. The notation "+" indicates that the energy difference between the two term symbols is too small to be shown. The notation "/" indicates that the term symbols are degenerate.

DOI: 10.1021/acs.inorgchem.6b01228
Inorg. Chem. 2016, 55, 10152–10160

distortion of the Co ion. The first two excited states $^4T_2$ and $^4T_1$ further branch into four excited states, $^4B_2$, ^4E, $^4A_2$, and ^4E. The obtained distortion parameters are $D_s = -0.08$ eV and $D_t = 0.005$ eV. The application of 3d spin−orbit coupling (66 meV) gives rise to two double-degenerate Γ_6 and Γ_7 states, branched from the $^4B_1$ ground state, which are the Kramer's doublets. Note that Figure 7 is an incomplete picture in which the compositions of each energy level, as well as the energy branching, are assumed to be 100% pure without mixing. Such an assumption is improper and can hardly explain the splitting of the $^4B_1$ and $^4B_2$ states into Γ_6 and Γ_7 states due to the 3d spin−orbit coupling. A more realistic demonstration of the compositions and branchings of microstates is discussed in the section below.

Wave-Function Decomposition. The detailed wave-function descriptions of the compound ground state and a few excited states are presented in Table 2 under different point group symmetries. All calculations were performed based on the ligand-field multiplet parameters listed in Table 1. In spherical SO_3 symmetry, all atomic states are described by pure atomic term symbols, with the exception that the ^2D term symbol occurs twice and each ^2D state is a linear combination of both. We discriminate the different symbols as ^2_aD and ^2_bD. Note that the energies of the ^2P and ^2H manifolds are intrinsically degenerate.[48] When a tetrahedral ligand field (here $10D_q = -0.54$ eV) is applied, the ^4F ground state is split into $^4A_2$, $^4T_2$, and $^4T_1$ states. The first two manifolds are pure in ^4F character (if 3d spin−orbit coupling is neglected) because they are the only $^4A_2$ and $^4T_2$ states of the $3d^7$ manifold. The $^4T_1$ state contains ∼3% ^4P character due to the mixing of two $^4T_1$ symmetry states. Similarly, in the one-electron orbital descriptions, the $^4A_2$ and $^4T_2$ states are both pure and with an $e^4t_2^3$ and an $e^3t_2^4$ occupation each, while the $^4T_1$ multiplet contains 65.8% $|e^2t_2^5\rangle$ and 34.2% $|e^3t_2^4\rangle$.

Changing the T_d symmetry to D_{2d} symmetry, the $^4A_2$ ground state branches into the $^4B_1$ state, which retains its pure ^4F character and a corresponding pure $|e^2b_2^1a_1^2b_1^2\rangle$ one-electron orbital description. The pure $^4T_2$ state branches into a pure $^4B_2$ state and a ^4E state, which mixes with another ^4E state, turning it into a complex mixed orbital description. The main component is the 84.6% $|e^3b_2^1a_1^1b_1^2\rangle$ state that can be understood as all spin-up electrons occupied plus a spin-down electron in each of the e and b_1 orbitals. The remaining ∼15% of this ^4E state contains other distributions of electrons over the e, b_2, a_1, and b_1 orbitals (cf. Table 2). Furthermore, apart from the main compositions, a 2.9% $|^4T_1\rangle$ cubic symmetry or a 0.5% $|^4P\rangle$ atomic term symbol character is found for this ^4E state. Switching on the 3d spin−orbit coupling gives rise to assignments in double group notations Γ_6 and Γ_7. Most importantly, with the inclusion of 3d spin−orbit coupling, the $^4B_1$ ground state is not a pure quartet state anymore, but an approximate 0.2% doublet character is mixed. In the orbital composition, the effects of 3d spin−orbit coupling are larger, which leads to around 2% states with different orbital compositions to mix into the ground state. As can be seen in the last column, these 2% states are mainly related to the $^4T_2$ excited configuration, which mix via the 3d spin−orbit coupling.

CONCLUSIONS

Co $2p_{3/2}$ XAS and 2p3d RIXS spectra were acquired for the sample $K_5H[CoW_{12}O_{40}]\cdot xH_2O$. The high-energy resolution (∼0.09 eV fwhm) Co 2p3d RIXS data of the single-cobalt-centered POM $K_5H[CoW_{12}O_{40}]\cdot xH_2O$ is reported for the first time, which experimentally revealed the UV/vis unmeasurable low-energy dd transition features. The experimental XAS and RIXS spectra were adequately reproduced with ligand-field multiplet simulations by considering the temperature-dependent occupation of the excited states. In fact, these data represent the first reported tetrahedral-like Co^{II} soft RIXS data. The ligand-field multiplet data simulations also allowed an effective discussion about the potential Co site tetragonal distortion. Parameters accounting for the ligand field on the Co ion have strengths of $10D_q = -0.54$ eV, $D_s = -0.08$ eV, and $D_t = 0.005$ eV. An improved experimental resolution is still required though to be conclusive on this topic. The ligand-field multiplet RIXS simulation addressed the labeling of a few observed dd features, and it also enabled a comparison with previous dd transition assignments from optical data and DFT calculations. Because RIXS clearly demonstrated both optical spin-allowed and -forbidden transitions, the current dd featured assignments show a higher accuracy. The wave-function decomposition analyses, using ligand-field multiplet projection methods, provided realistic and detailed origins of each dd transition, both from one-electron-orbital and term-symbol descriptions. In conclusion, the high-energy resolution Co 2p3d RIXS spectra and ligand-field multiplet simulations offered unprecedented information on the cobalt electronic structure in $K_5H[CoW_{12}O_{40}]\cdot xH_2O$, suggesting further applications of this technique to explore the potential WOC activity-related cobalt electronic structures in different cobalt-containing POMs.

ASSOCIATED CONTENT

Supporting Information

The Supporting Information is available free of charge on the ACS Publications website at DOI: 10.1021/acs.inorgchem.6b01228.

Explanation of the AGM−AGS system and energy calibration in the current work, UV/vis and FT-IR spectra of $K_5H[CoW_{12}O_{40}]\cdot 12H_2O$, a detailed description of the ligand-field multiplet XAS and RIXS calculations and justification of the applied parameters, and Boltzmann-weighted RIXS simulation of cross sections at excitation energies b, c, and e (PDF)

X-ray crystallographic data in CIF format (CIF)

AUTHOR INFORMATION

Corresponding Authors

*E-mail: M.M.vanSchooneveld@uu.nl.

*E-mail: F.M.F.deGroot@uu.nl.

Notes

The authors declare no competing financial interest.

ACKNOWLEDGMENTS

This work was financially supported by the China Scholarship Council and the ERC advanced grant XRAYonACTIVE (Grant 340279). We thank Wenbin Wu in the NSRRC for technical support.

REFERENCES

(1) Khodakov, A. Y.; Chu, W.; Fongarland, P. *Chem. Rev.* **2007**, *107*, 1692−1744.

DOI: 10.1021/acs.inorgchem.6b01228
Inorg. Chem. 2016, 55, 10152−10160

(2) Matsumoto, Y.; Murakami, M.; Shono, T.; Hasegawa, T.; Fukumura, T.; Kawasaki, M.; Ahmet, P.; Chikyow, T.; Koshihara, S.; Koinuma, H. *Science* **2001**, *291*, 854−856.
(3) Yin, Q. S.; Tan, J. M.; Besson, C.; Geletii, Y. V.; Musaev, D. G.; Kuznetsov, A. E.; Luo, Z.; Hardcastle, K. I.; Hill, C. L. *Science* **2010**, *328*, 342−345.
(4) Huang, Z. Q.; Luo, Z.; Geletii, Y. V.; Vickers, J. W.; Yin, Q. S.; Wu, D.; Hou, Y.; Ding, Y.; Song, J.; Musaev, D. G.; Hill, C. L.; Lian, T. Q. *J. Am. Chem. Soc.* **2011**, *133*, 2068−2071.
(5) Lv, H. J.; Song, J.; Geletii, Y. V.; Vickers, J. W.; Sumliner, J. M.; Musaev, D. G.; Kogerler, P.; Zhuk, P. F.; Bacsa, J.; Zhu, G. B.; Hill, C. L. *J. Am. Chem. Soc.* **2014**, *136*, 9268−9271.
(6) Lv, H. J.; Geletii, Y. V.; Zhao, C. C.; Vickers, J. W.; Zhu, G. B.; Luo, Z.; Song, J.; Lian, T. Q.; Musaev, D. G.; Hill, C. L. *Chem. Soc. Rev.* **2012**, *41*, 7572−7589.
(7) Nomiya, K.; Miwa, M.; Kobayashi, R.; Aiso, M. *Bull. Chem. Soc. Jpn.* **1981**, *54*, 2983−2987.
(8) Kojima, K.; Matsuda, J. *Bull. Chem. Soc. Jpn.* **1985**, *58*, 821−825.
(9) Glass, E. N.; Fielden, J.; Kaledin, A. L.; Musaev, D. G.; Lian, T. Q.; Hill, C. L. *Chem. - Eur. J.* **2014**, *20*, 4297−4307.
(10) Schiwon, R.; Klingan, K.; Dau, H.; Limberg, C. *Chem. Commun.* **2014**, *50*, 100−102.
(11) Hibberd, A. M.; Doan, H. Q.; Glass, E. N.; de Groot, F. M. F.; Hill, C. L.; Cuk, T. *J. Phys. Chem. C* **2015**, *119*, 4173−4179.
(12) van Schooneveld, M. M.; Gosselink, R. W.; Eggenhuisen, T. M.; Al Samarai, M.; Monney, C.; Zhou, K. J. J.; Schmitt, T.; de Groot, F. M. F. *Angew. Chem., Int. Ed.* **2013**, *52*, 1170−1174.
(13) de Groot, F. M. F. *Coord. Chem. Rev.* **2005**, *249*, 31−63.
(14) Waegele, M. M.; Doan, H. Q.; Cuk, T. *J. Phys. Chem. C* **2014**, *118*, 3426−3432.
(15) Magnuson, M.; Butorin, S. M.; Guo, J. H.; Nordgren, J. *Phys. Rev. B: Condens. Matter Mater. Phys.* **2002**, *65*, 205106.
(16) Maestre, J. M.; Lopez, X.; Bo, C.; Poblet, J. M.; Daul, C. *Inorg. Chem.* **2002**, *41*, 1883−1888.
(17) Glass, E. N.; Fielden, J.; Huang, Z. Q.; Xiang, X.; Musaev, D. G.; Lian, T. Q.; Hill, C. L. *Inorg. Chem.* **2016**, *55*, 4308−4319.
(18) van Schooneveld, M. M.; Kurian, R.; Juhin, A.; Zhou, K. J.; Schlappa, J.; Strocov, V. N.; Schmitt, T.; de Groot, F. M. F. *J. Phys. Chem. C* **2012**, *116*, 15218−15230.
(19) Lai, C. H.; Fung, H. S.; Wu, W. B.; Huang, H. Y.; Fu, H. W.; Lin, S. W.; Huang, S. W.; Chiu, C. C.; Wang, D. J.; Huang, L. J.; Tseng, T. C.; Chung, S. C.; Chen, C. T.; Huang, D. J. *J. Synchrotron Radiat.* **2014**, *21*, 325−332.
(20) Fung, H. S.; Chen, C. T.; Huang, L. J.; Chang, C. H.; Chung, S. C.; Wang, D. J.; Tseng, T. C.; Tsang, K. L. *AIP Conf. Proc.* **2003**, *705*, 655−658.
(21) Ghiringhelli, G.; Brookes, N. B.; Annese, E.; Berger, H.; Dallera, C.; Grioni, M.; Perfetti, L.; Tagliaferri, A.; Braicovich, L. *Phys. Rev. Lett.* **2004**, *92*, 117406.
(22) Kuiper, P.; Guo, J. H.; Sathe, C.; Duda, L. C.; Nordgren, J.; Pothuizen, J. J. M.; de Groot, F. M. F.; Sawatzky, G. A. *Phys. Rev. Lett.* **1998**, *80*, 5204−5207.
(23) Cowan, R. D. *J. Opt. Soc. Am.* **1968**, *58*, 808−818.
(24) Cowan, R. D. *The Theory of Atomic Structure and Spectra*; University of California Press: Berkeley, CA, 1981.
(25) Thole, B. T.; van der Laan, G.; Butler, P. H. *Chem. Phys. Lett.* **1988**, *149*, 295−299.
(26) de Groot, F. M. F.; Kotani, A. *Core Level Spectroscopy of Solids*; CRC Press: Boca Raton, FL, 2008.
(27) Stavitski, E.; de Groot, F. M. F. *Micron* **2010**, *41*, 687−694.
(28) de Groot, F. M. F.; Fuggle, J. C.; Thole, B. T.; Sawatzky, G. A. *Phys. Rev. B: Condens. Matter Mater. Phys.* **1990**, *41*, 928−937.
(29) Wasinger, E. C.; de Groot, F. M. F.; Hedman, B.; Hodgson, K. O.; Solomon, E. I. *J. Am. Chem. Soc.* **2003**, *125*, 12894−12906.
(30) Delgado-Jaime, M. U.; Zhang, K.; Vyra-Weis, J.; de Groot, F. M. F. *J. Synchrot. Rad.* **2016**, *23*, 1264−1271.
(31) Haverkort, M. W.; Sangiovanni, G.; Hansmann, P.; Toschi, A.; Lu, Y.; Macke, S. *Europhys. Lett.* **2014**, *108*, 57004.
(32) Haverkort, M. W.; Zwierzycki, M.; Andersen, O. K. *Phys. Rev. B: Condens. Matter Mater. Phys.* **2012**, *85*, 165113.
(33) Hariki, A.; Ichinozuka, Y.; Uozumi, T. *J. Phys. Soc. Jpn.* **2013**, *82*, 043710.
(34) Hariki, A.; Yamanaka, A.; Uozumi, T. *J. Phys. Soc. Jpn.* **2015**, *84*, 073706.
(35) Roemelt, M.; Maganas, D.; DeBeer, S.; Neese, F. *J. Chem. Phys.* **2013**, *138*, 204101−204122.
(36) Maganas, D.; Roemelt, M.; Hävecker, M.; Trunschke, A.; Knop-Gericke, A.; Schlögl, R.; Neese, F. *Phys. Chem. Chem. Phys.* **2013**, *15*, 7260−7276.
(37) Lundberg, M.; Kroll, T.; DeBeer, S.; Bergmann, U.; Wilson, S. A.; Glatzel, P.; Nordlund, D.; Hedman, B.; Hodgson, K. O.; Solomon, E. I. *J. Am. Chem. Soc.* **2013**, *135*, 17121−17134.
(38) Pinjari, R. V.; Delcey, M. G.; Guo, M. Y.; Odelius, M.; Lundberg, M. *J. Chem. Phys.* **2014**, *141*, 124116.
(39) Suljoti, E.; Garcia-Diez, R.; Bokarev, S. I.; Lange, K. M.; Schoch, R.; Dierker, B.; Dantz, M.; Yamamoto, K.; Engel, N.; Atak, K.; Kühn, O.; Bauer, M.; Rubensson, J.-E.; Aziz, E. F. *Angew. Chem., Int. Ed.* **2013**, *52*, 9841−9844.
(40) Kramers, H. A.; Heisenberg, W. *Z. Phys.* **1925**, *31*, 681−708.
(41) de Groot, F. M. F. *Phys. Rev. B: Condens. Matter Mater. Phys.* **1996**, *53*, 7099−7110.
(42) Casanpastor, N.; Gomezromero, P.; Jameson, G. B.; Baker, L. C. W. *J. Am. Chem. Soc.* **1991**, *113*, 5658−5663.
(43) Cramer, S. P.; de Groot, F. M. F.; Ma, Y.; Chen, C. T.; Sette, F.; Kipke, C. A.; Eichhorn, D. M.; Chan, M. K.; Armstrong, W. H.; Libby, E.; Christou, G.; Brooker, S.; McKee, V.; Mullins, O. C.; Fuggle, J. C. *J. Am. Chem. Soc.* **1991**, *113*, 7937−7940.
(44) Stöhr, J. *NEXAFS Spectroscopy*, 1st ed.; Springer-Verlag: New York, 1992; Vol. *25*.
(45) van Schooneveld, M. M.; DeBeer, S. *J. Electron Spectrosc. Relat. Phenom.* **2015**, *198*, 31−56.
(46) Ament, L. J. P.; van Veenendaal, M.; Devereaux, T. P.; Hill, J. P.; van den Brink, J. *Rev. Mod. Phys.* **2011**, *83*, 705−767.
(47) Nataf, L.; Rodriguez, F.; Valiente, R.; Ulanov, V. *J. Lumin.* **2009**, *129*, 1602−1605.
(48) Oliva, J. M. *Phys. Lett. A* **1997**, *234*, 41−44.
(49) Pisarev, R. V.; Kalashnikova, A. M.; Schops, O.; Bezmaternykh, L. N. *Phys. Rev. B: Condens. Matter Mater. Phys.* **2011**, *84*, 075106.
(50) Shannon, R. D. *Acta Crystallogr., Sect. A: Cryst. Phys., Diffr., Theor. Gen. Crystallogr.* **1976**, *32*, 751−767.

DOI: 10.1021/acs.inorgchem.6b01228
Inorg. Chem. 2016, 55, 10152−10160